THE BELL SYSTEM TECHNICAL JOURNAL
Vol. 56, No. 4, April 1977
Printed in U.S.A.

On the Occurrence of Caustics in the Drawdown Zone of Silica Fibers

By P. G. SIMPKINS, T. D. DUDDERAR, J. McKENNA and J. B. SEERY

(Manuscript received September 16, 1976)

Caustics created by internal reflections and interface refraction have been observed in the molten drawdown zones of fibers during manufacture in a laser furnace. These regions of high luminescence are associated with the rapid change in cross-sectional area that occurs in the drawdown zone. Observations made with solidified samples of the molten drawdown zone reveal the nature of the caustic envelopes. Algorithms which incorporate ray tracing techniques have been developed and used with surface profile measurements to generate caustic loci. The results from these numerical experiments are in good agreement with observations. The caustics are found to be particularly sensitive to asymmetries in the drawdown profile. A simple technique for monitoring the maximum gradient of the drawdown zone is also described.

I. INTRODUCTION

The drawdown zone of a silica fiber manufactured in a laser furnace has a cross section that varies rapidly along its axis. When this zone is internally illuminated with a collimated beam parallel to the axis, a region of high-intensity radiation is observed (see Fig. 1). The radiation is the result of multiple internal reflections and a refraction of the beam caused by the rapidly varying boundary of the glass. The locus where the rays of geometrical optics form an envelope is known as a caustic. Along such a surface the luminous intensity is a maximum.[1] Normal to the caustic, the intensity is characterized mathematically by an Airy function, decaying exponentially on one side, the shadow region, and varying harmonically in the opposite direction. For simple geometries, the techniques used to calculate the caustics are straightforward; e.g., a collimated beam reflected from a semicircular concave mirror forms a caustic which is part of an epicycloid. When the reflecting boundaries

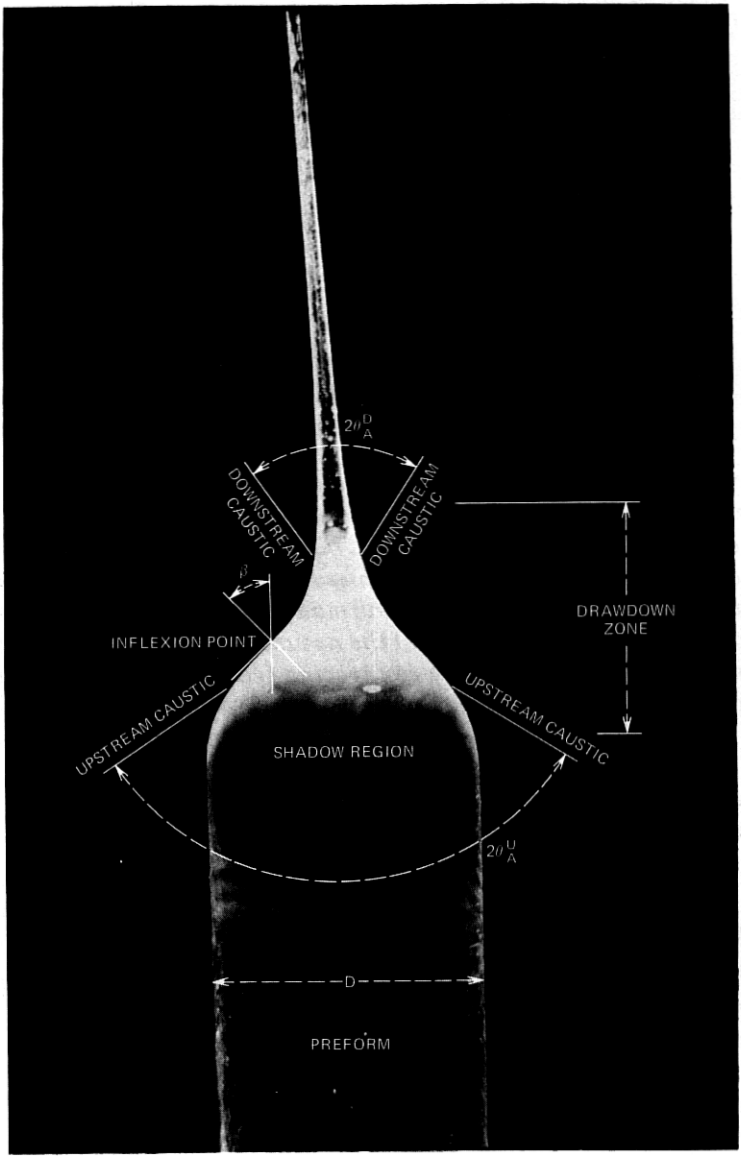

Fig. 1—High-intensity drawdown zone labeled with the relevant geometrical parameters.

are not given analytically, however, the calculation of the caustic geometry is more laborious.

It is our hypothesis that light reflected and refracted from the drawdown zone in the form of caustics can provide an extremely sensitive measure of the surface geometry and, possibly, such physical quantities

as the index of refraction and temperature. Observations made during an actual silica-fiber drawing operation confirm the existence of caustics in the molten zone. In that case, the emission is the result of the high-intensity radiation along numerous ray paths, many of which are skewed.

In this paper, we restrict our attention to an examination of the solidified drawdown zones of a number of fused-silica samples. For the most part, we concentrate on the radiation produced by an internal plane wave traveling along a sample; this is not, however, a limitation as experiments with a diffused source will show. Our observations are used to illustrate that the caustics originate from light rays traveling through different regions within the cross section. Furthermore, we show that the drawdown contour plays an important role in defining the caustic geometry and that small changes in the profile gradient can produce large variations in the caustic patterns. For a given index of refraction, ray theoretic analysis and geometrical optics confirm that the observed far-field caustic phenomenon can be predicted with good accuracy provided the boundary of the drawdown zone is well defined. Conversely, careful observation of the caustic patterns might be used to determine important aspects of the drawdown zone's geometry. We also show that a reflected caustic generated by external illumination of the drawdown zone may be used to provide a practical and accurate measure of the maximum profile gradient.

We consider two limiting cases and describe these as an "upstream" and a "downstream" caustic, in order to designate their nominal location relative to the silica flow during the drawing operation. These caustics do not appear in the drawdown zone of preforms being heated in an induction furnace since the profile gradient is too small. However, a geometrically relevant caustic can always be generated by external illumination of the drawdown zone regardless of how small the profile gradient becomes. This point will be discussed further below.

II. EXPERIMENTAL METHODS

Solidified samples of the transition region between the preform and the fiber were cut and polished square to the axis on the preform end some 50 mm ahead of the drawdown zone. Each sample began at a preform of a uniform diameter between 6.5 mm and 8 mm, and terminated at a fiber diameter of typically 200 μm.* All the samples were of fused silica with an index of refraction, n, of 1.457 at a wavelength of 643.8 nm.[2] Individual samples were mounted in a gimballed mirror mount with micrometer adjustment. The sample was usually illuminated internally

* Although the drawdown region continues much further—to a final fiber diameter of about 100 μm—this region is of no interest to the current study.

by a light beam entering the preform parallel to the fiber axis. This technique generated the upstream and downstream caustics. The sample could also be illuminated externally by a beam normal to the fiber axis and incident to the drawdown zone. This alternative generated a reflected caustic from which the maximum gradient of the drawdown profile could be determined. An Argon Ion or He-Ne laser, $\lambda = 514.5$ and 632.8 nm, respectively, provided the illumination. In either case, the beam was expanded through a spatial filter and collimated to a diameter greater than the preform. Particular regions of the preform cross section were selectively illuminated via adjustable slits and diaphragms. When required, the collimated beam was altered by introducing a diffuser at the polished end of the sample. The experimental arrangement is illustrated in Fig. 2.

Images of the caustic patterns emitted from a particular sample were recorded in planes parallel and perpendicular to its axis. These far-field caustic images (see Figs. 3 and 4 for typical examples) were obtained by mounting the film in a Polaroid* film holder and exposing it in a darkened room, or, by photographing the image formed on a suitable screen in the same plane. By translating the sample relative to the reference plane, the locus and orientation of the caustic was determined. The precise location of the caustic at the surface of the sample was obtained by adjusting a toolmaker's height gauge, in contact with the surface, until it interrupted the display of the far-field caustic image.

III. EXPERIMENTAL RESULTS

3.1 Origins of the caustics

A diaphragm aperture was used to vary the incident-beam diameter to determine which annular regions within a transverse cross section of the sample transmitted light that contributed to each caustic. With a ground glass viewing screen in position 1 or 3, Fig. 2, the incident beam diameter was reduced until the caustics disappeared. Figure 3 shows typical far-field photographs taken during these tests. When the beam and preform diameters were equal, both upstream and downstream caustics were visible. When the beam diameter was reduced approximately five percent, the downstream caustic vanished, while the upstream caustic remained unaffected. The upstream caustic remained intense until the beam diameter was reduced to between 60 and 55 percent of the sample diameter, when it began to lose intensity rapidly. These observations show that the downstream caustic originates from a region very near the shoulder of the drawdown. The upstream caustic has its source close to the inflexion point of the drawdown zone.

When the image plane was oriented parallel to the preform axis, po-

* Registered trademark of Polaroid Corporation.

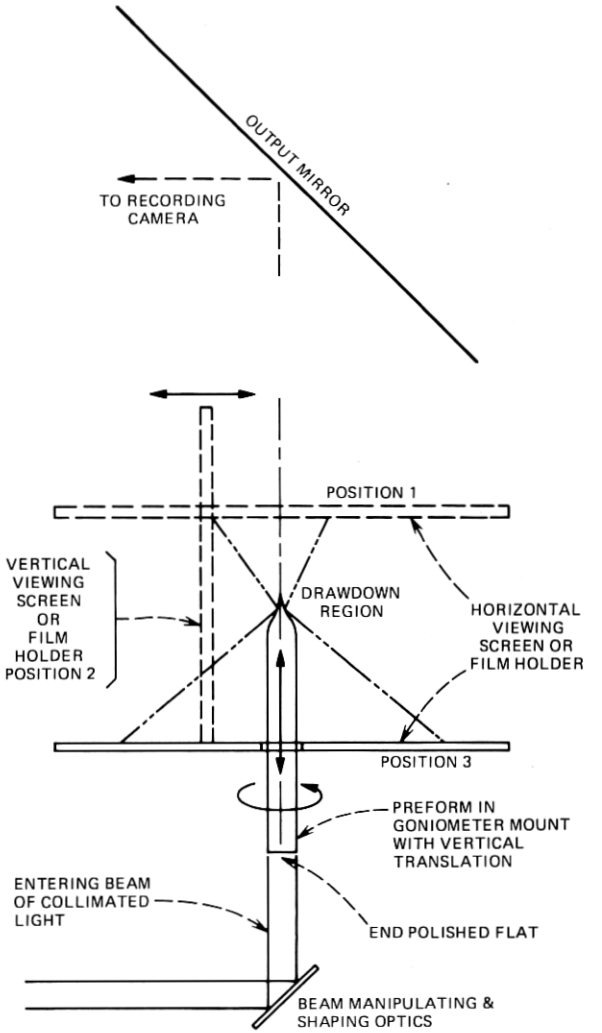

Fig. 2—Experimental arrangements for measuring various caustic loci.

sition 2 in Fig. 2, the caustic pattern for a symmetric sample became hyperbolas. The photographs in Fig. 4 show a comparison of the caustic images recorded using beams of different diameters with and without a diffuser. The principal observation is that both caustics can be seen in the full beam photographs. Although the detailed structure that occurs with the collimated beam has been eliminated by the diffuser, the skew rays introduced thereby do not eliminate the caustics. A reduction in the collimated beam diameter below that of the preform quickly eliminates the downstream caustics. However, they can still be seen whenever

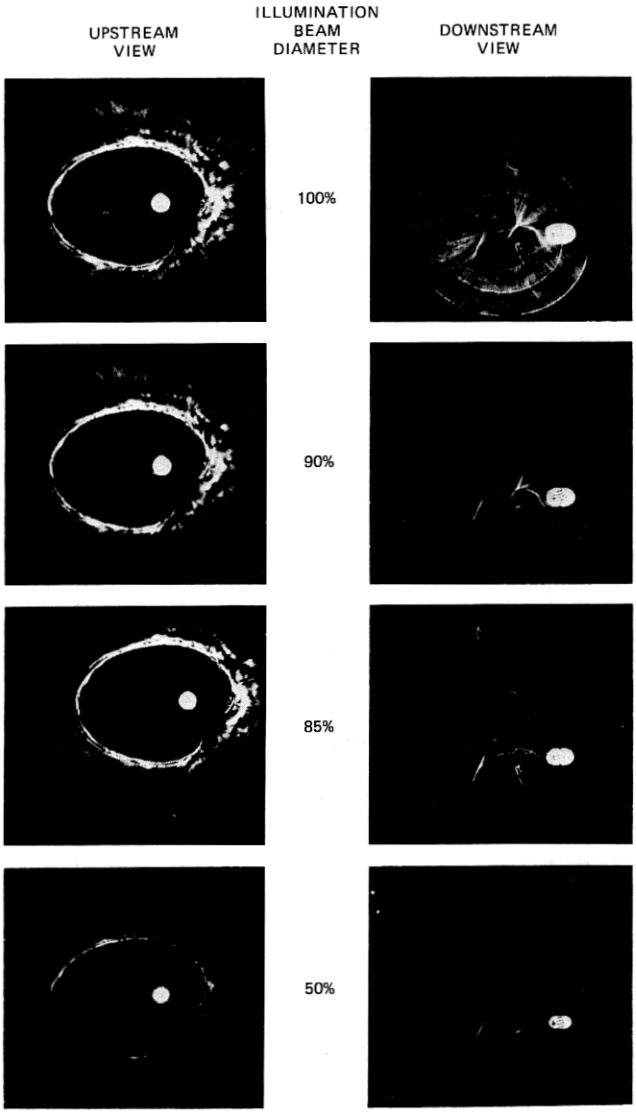

Fig. 3—Variations of the far-field caustic images (positions 1 and 3) with changes in illuminating-beam diameter; sample 1.

the diffuser is placed in the beam because the light scattered towards the surface can be reflected to form the downstream caustic. Significantly, as the beam is stopped down further, so that the upstream caustic also starts to disappear, the resolution of both caustics becomes relatively more apparent with the diffused beam. Considerable additional caustic structure, which is completely obscured in the patterns recorded with

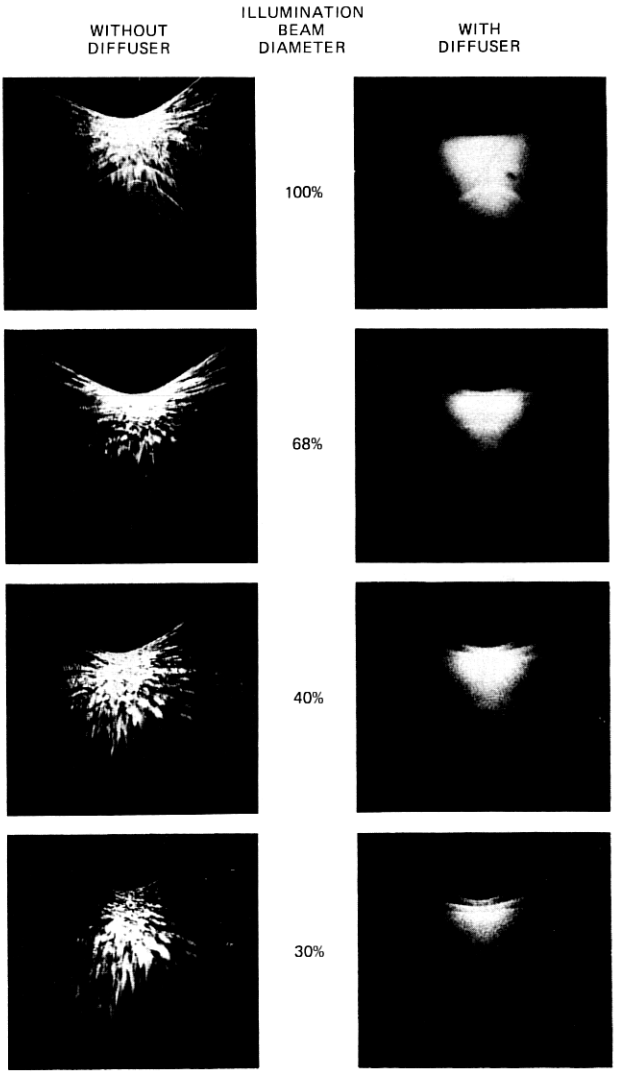

Fig. 4—Variations of the far-field caustic images (position 2) with collimated and diffused illuminating beams of changing diameter side views.

the fully collimated beam, becomes visible in patterns recorded over much longer times with diffused beams of substantially reduced diameter.

3.2 Propagation paths of the emergent caustics

Accurate* determinations of the propagation directions of the caustics

* See Appendix for estimates of accuracy.

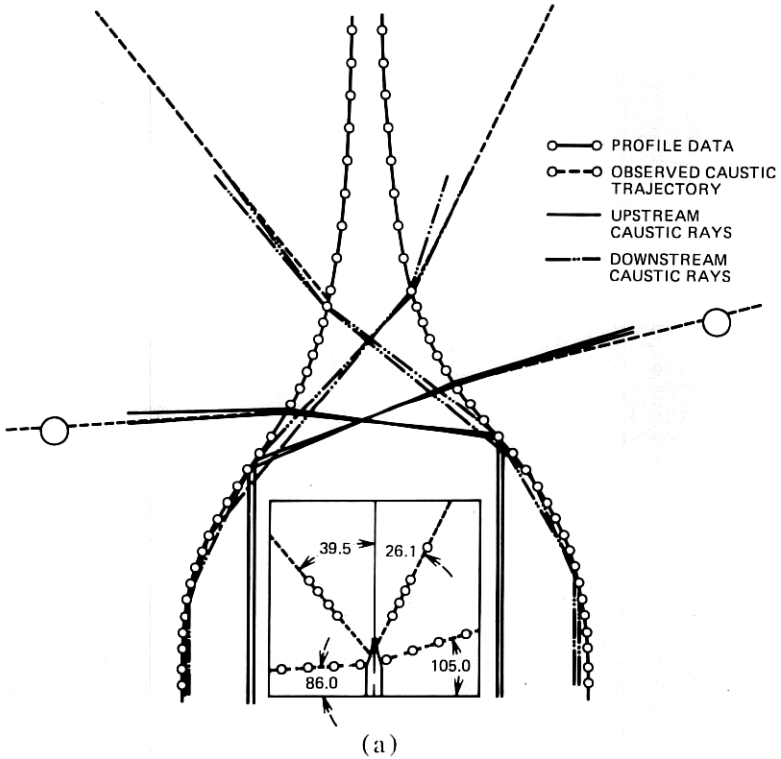

Fig. 5—(a) Comparison of the measured far-field caustic trajectories and the graphical ray traces for adjacent rays bounding the caustic ray.

and the precise loci of their emergence from the preform were made as described in Section II. This information was subsequently compared with emerging caustics identified by geometrical ray tracing through a known preform geometry. The ray tracing was performed graphically on a fiftyfold enlargement. Figure 5a shows, on a necessarily reduced scale, the excellent agreement between the experimental observation and the graphical ray tracing in a typical sample, such as sample 4.

From the above comparisons, we conclude that the observed caustics do indeed result from light following the paths determined by the graphical ray tracing. In Fig. 5a we see that the upstream caustic is generated by rays traveling down the sample at about the half radius which reflect internally once. These rays then cross the sample and strike the diametrically opposite side at such an angle that they emerge upstream of the downstream caustics. A caustic represents a limiting phenomenon at which the field of emerging refracted rays folds back upon itself. Thus, the upstream caustic represents the furthermost up-

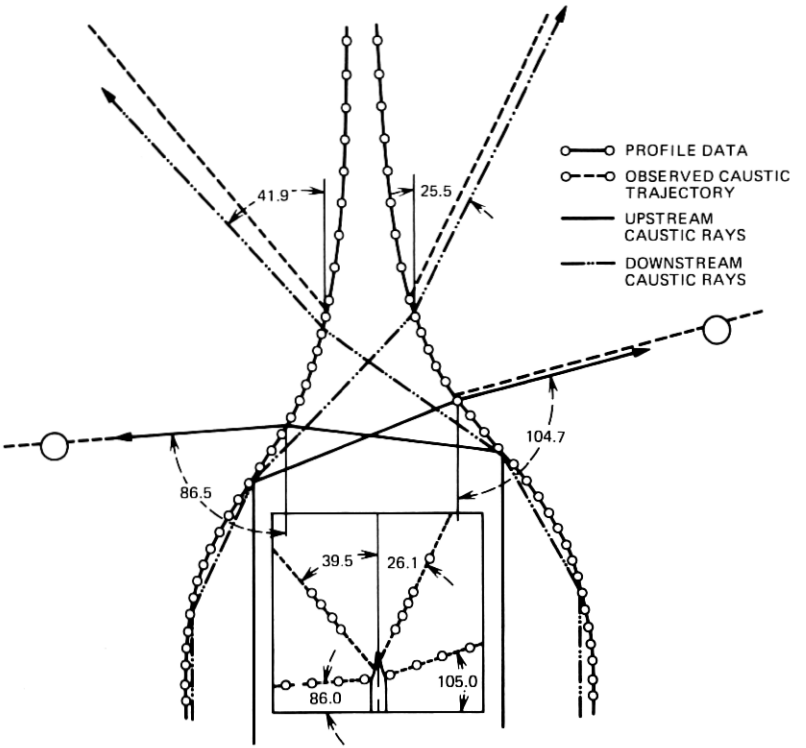

(b)

Fig. 5—(b) Comparison of the same observations with the numerical calculations.

stream limit that rays can emerge from the preform. It is possible, however, that the upstream caustic will not appear because the field of emerging rays is terminated at the critical angle. Then, before the field can fold back upon itself, it is internally reflected. The upstream image for such a condition is shown in Fig. 6b where no caustic is seen at the boundary between the light and dark regions. A similar internal reflection occurs locally with the original sample shown in Fig. 3. The asymmetry of the caustic observed in Fig. 3 and its local extinction are due to asymmetries in the drawdown profile, the effects of which will be discussed in Section 3.3.

Referring now to the downstream caustics, we have already established in Section 3.1 that these arise from light traveling down the sample very close to its surface. Their behavior is similar to the upstream caustic; however, the graphical ray tracing reveals an important distinction between the two families. The downstream caustic is formed by rays that have reflected twice before crossing the sample and emerging (see Fig. 5a). As noted earlier, there is excellent agreement between the constructed and observed caustic locations. This caustic is unique in that

Table I — Synopsis of the drawdown sample geometries

Sample	Station	Taper L/D*	$\gamma = \left(\frac{dy}{dx}\right)_{max}$	$\beta = \text{arc cot } \gamma$
1	3	0.73	0.87	48.9°
	6	0.73	0.92	47.3°
	9		1.01	44.6°
	12		0.98	45.6°
2	3	0.62	1.02	44.5°
	6	0.63	1.12	41.7°
	9		1.05	43.5°
	12		0.99	45.2°
3	3	0.44	1.95	27.1°
	6	0.46	1.89	27.9°
	9		1.89	27.9°
	12		2.14	25.0°
4	3	0.94	0.82	50.6°
	6	0.97	0.67	56.0°
	9		0.72	54.2°
	12		0.88	48.8°

* The taper information relates to pairs of profiles, so the information in row 3 refers to profiles 3 and 9 while information in row 6 refers to profiles 6 and 12.

no other ray paths give rise to a downstream caustic with a greater cone angle.

3.3 Studies of geometrical effects

3.3.1 Upstream caustics

Four samples with different geometries were studied to develop an understanding of the relationship between the shape of the drawdown region and the caustic loci. These samples, described in Table I, were selected to span the range of geometries to be expected from the laser drawing process. Every sample was examined in two orthogonal planes, parallel to the axis. These planes intersect the drawdown zone in four curves labelled 3, 6, 9 and 12 when viewed from the fiber end. The drawdown taper (L/D) ranges from $0.4 \leqq L/D \leqq 1.0$. Here D is the preform diameter, and L is the distance along the axis from a diameter of 0.98D to one of 0.15D. The maximum gradient, $\gamma = (dy/dx)_{max}$, ranged from 0.67 to 2.14. Since the caustic formation depends upon interactions between the ray trajectories and opposite boundaries of the drawdown zone, asymmetries on any particular cross section are of considerable significance.

The most extensive studies were made on sample 1 and have been discussed earlier. The other three samples were examined only with a full collimated beam (see Fig. 2) to establish the caustic geometries. Typical far-field caustic patterns from each sample are given in Figs. 6 and 7. The upstream images (see Fig. 6) illustrate the diversity of patterns that arise because of variations in the profile geometry. Figure 6a

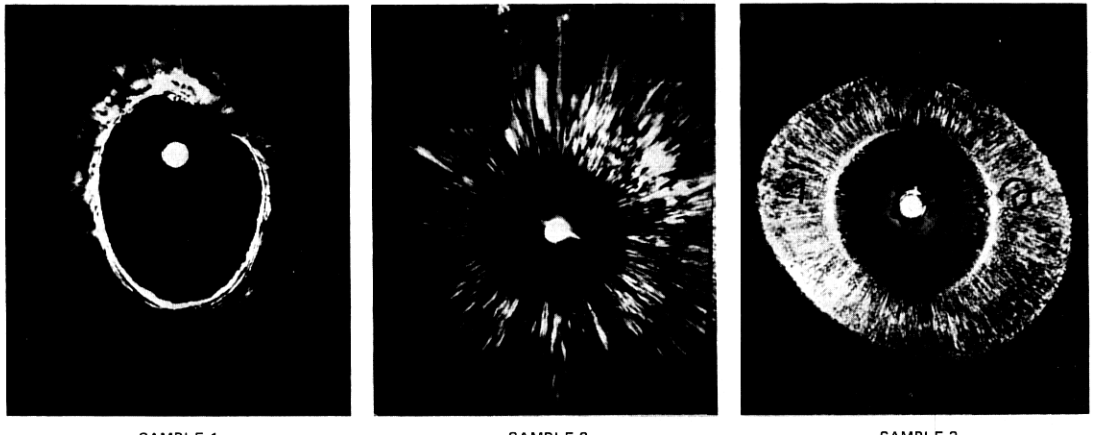

SAMPLE 1 (A) SAMPLE 2 (B) SAMPLE 3 (C)

UPSTREAM VIEW

Fig. 6—Far-field upstream (position 3) caustic images observed from three different samples, illustrating the effects of geometrical variations.

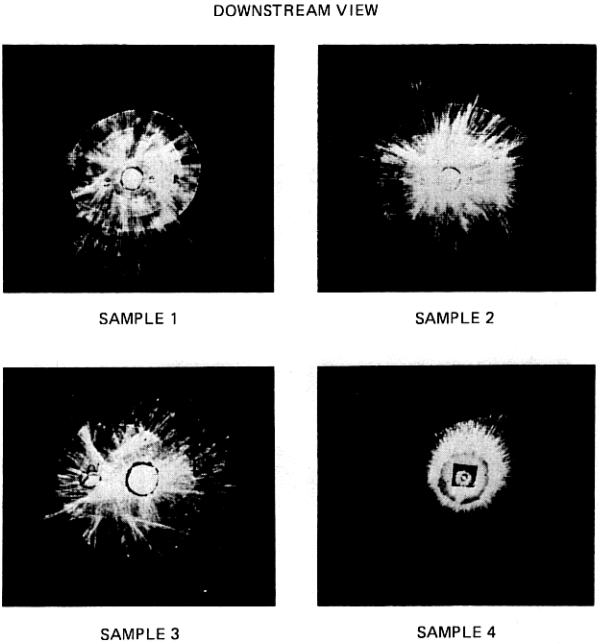

Fig. 7—Far-field downstream (position 1) caustic images observed from four different samples.

shows a single caustic with considerable asymmetry, one segment of which vanishes where internal reflection occurs. Figure 6b shows an occurrence in which there are no upstream caustics, which is again the result of internal reflection. Referring to Table I, we note that the angles of the normals to the profile, β, for samples 1 and 2 are in the neighborhood of 45°. Here $\beta = \text{arc cot } \gamma$. Since the upstream caustic ray paths intercept each boundary once, this assures that the significant incident rays approach the second surface at angles close to the critical value of 43.2° ($n = 1.46$). In these circumstances, the ray trajectories for sample 1 are such that the incident angle, ϕ, is usually less than, but close to, the critical angle. On the other hand, for sample 2, ϕ is everywhere greater than the critical angle. Snell's law predicts an increased sensitivity of the refracted ray to changes in the incident ray path in the vicinity of the critical angle; this is illustrated in Fig. 8. Clearly in regions close to the critical angle small changes in incidence are magnified considerably. Thus, sample 1 shows large caustic eccentricity associated with modest profile asymmetry, while sample 2 exhibits no upstream caustic at all. It does, of course, exhibit a transition between dark and light regions in the upstream field. However, the locus of this transition is associated with the limiting rays of an internal reflection.

Consider now Fig. 6c, in which one observes the appearance of *two*

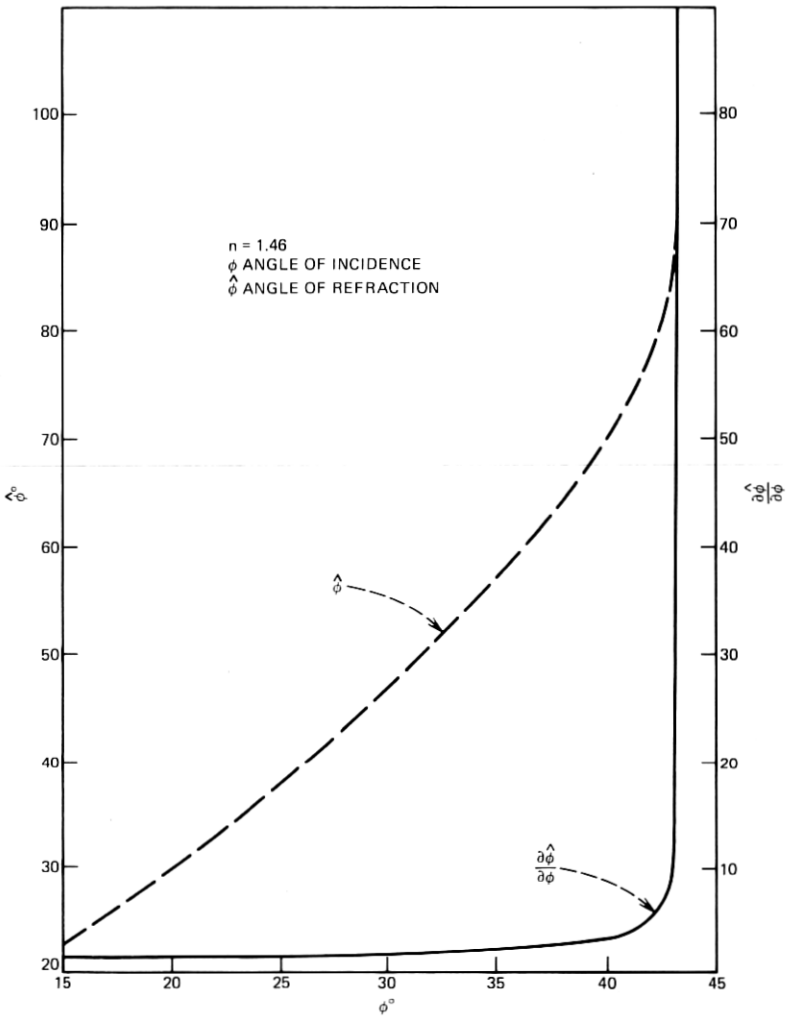

Fig. 8—Sensitivity of the angle of refraction, $\hat{\phi}$, to changes in the angle of incidence, ϕ, as ϕ approaches the critical angle.

upstream caustic boundaries. The condition arises because of the complicated reflections and refractions that occur in this sharply tapered drawdown region. The severity of the profile gradient allows some of the incident beam to refract from drawdown zone on the first interception with the boundary.* The small percentage of light that is internally reflected due to the low surface reflectance traverses the drawdown zone

* This emitted light forms a caustic at the inflexion point which is refracted downstream at a negative angle. This phenomenon is not classified as a 'downstream' caustic because it intercepts the drawdown surface only once before it is emitted.

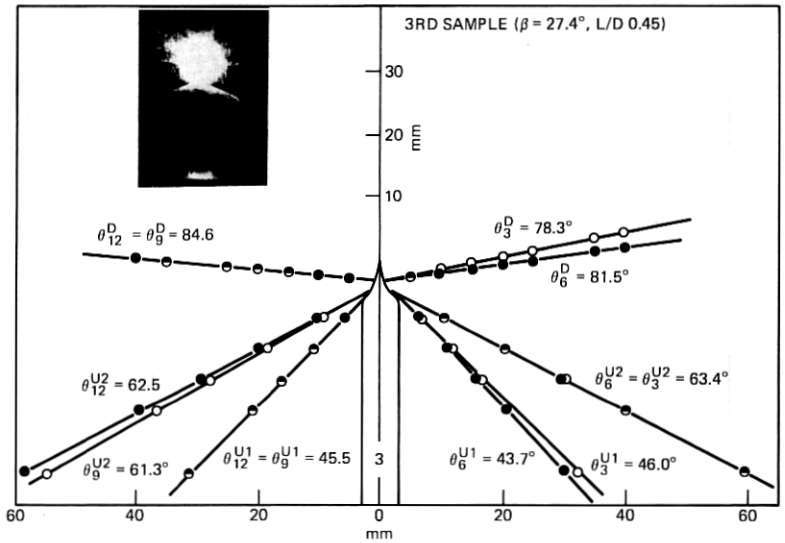

Fig. 9—Far-field caustic trajectories taken from sample 3, showing two upstream and a single downstream caustic. Each individual caustic can be identified on the accompanying photograph.

and emerges in the upstream direction bounded between two caustics (Fig. 6c).

Sample 4 is the shallowest of all those examined. Consequently, the ray trajectories are straightforward although the upstream caustic propagates downstream over an appreciable region of the polar angle. For that reason, no upstream photographs were made, and all data were recorded from position 2 (Fig. 2). Those measurements are given in the inserts of Fig. 5. The formation of the upstream caustic is the same as in sample 1, but since the local slope is much shallower, the incident ray angles are much less than the critical angle. Hence, the upstream caustic pattern for sample 4 is not as sensitive to deviations in the drawdown asymmetry.

3.3.2 Downstream caustics

Far-field images of the downstream caustics are shown in Fig. 7. The image for sample 3 is not apparent because it emerged almost normal to the axis. Data for this sample was therefore recorded from the side view, position 2, and is given in Fig. 9. Compared with the upstream caustics, the downstream ones are relatively well behaved and vary continuously with the surface geometry. The local caustic extinction found in the upstream cases does not now occur because the incident ray trajectories relative to the emergent surface are far removed from the critical angle. Careful analysis of these data shows that the downstream

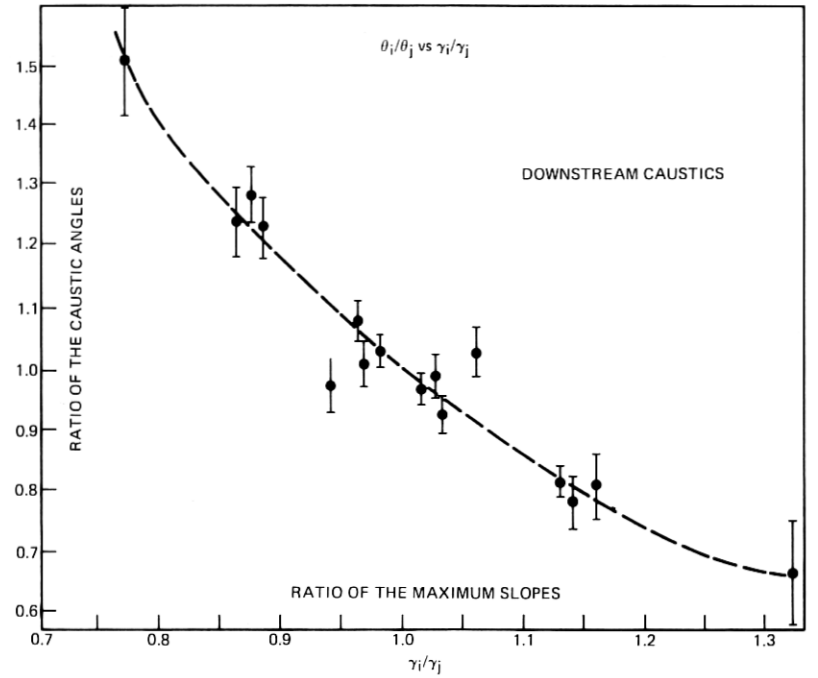

Fig. 10—Correlation of the downstream caustic angles with the maximum drawdown slope for all samples.

caustic asymmetry can be related to the asymmetry of the drawdown geometry. Figure 10 presents a correlation of the ratios of the caustic angles θ_i/θ_j, with the ratio of the maximum slopes γ_i/γ_j for all samples. The error bars represent the uncertainty in the measurement of the caustic angles, typically in absolute terms ±1°. With the exception of sample 3, the maximum gradients of the samples were obtained by spline fitting the original profile data measured with the Nikon comparator. The exterior reflected caustic technique was used to measure the gradient of sample 3 because its profile was too steep and irregular to be measured with the comparator and analyzed accurately. The significant aspect of the curve shown in Fig. 10 is the trend toward decreasing caustic angle ratio with increasing slope ratio. The scatter observed arises from the uncertainty in determining the slopes, and also from the probable dependence of the caustic asymmetry on factors other than the maximum gradient.

IV. MATHEMATICAL AND NUMERICAL ANALYSIS OF THE INTERNALLY ILLUMINATED CAUSTICS

In the preceding sections, we discussed the optical phenomena seen when the drawdown zone of a silica fiber is appropriately illuminated.

The experimental evidence presented shows that many important features of these phenomena could be explained by geometrical optics in terms of families of rays and their envelope curves or caustics. In this section, we derive equations for the rays in these families as well as equations for their caustic curves. These equations have been evaluated numerically, and we compare these numerical results with experimental results. Since the index of refraction of the glass is uniform, all the rays are straight lines between intercepts with the glass-air boundary. The continuation of a ray after its intercept with the boundary is determined by the laws of reflection and refraction of geometrical optics.[1] We assume that initially all rays are parallel to the axis of the preform, as is indicated in Fig. 11. A given initial ray in the preform and the axis of the perform determine a plane, called the initial plane. If the drawdown zone were axially symmetric, it is easily seen that at every reflection or refraction at the boundary, the ray would remain in that plane. In all the fibers we have considered, the drawdown zone is not axially symmetric. We have continued to make the approximation in our calculations, however, that any ray always remains in its initial plane. The good agreement between theory and experiment leads us to believe the error introduced by this approximation is small. Nevertheless, because the two curves in which the initial plane intersects the drawdown zone are different, any asymmetry of the drawdown is taken into account.

The derivation of the equations for the rays and the caustic curves is essentially the same for the double- and triple-intercept rays. As shown in Fig. 11, we express the boundary curves in the (ξ,η) coordinate system and the equations of the rays and caustics in the (x,y) coordinate system. A given ray is parameterized by the abscissa ξ of the point at which it first intercepts the boundary curve $g(\xi)$ of the drawdown zone. We then trace the ray until it emerges from the preform and write the equation of the emergent ray as

$$a(\xi)x + b(\xi)y = c(\xi). \tag{1}$$

Equation (1) represents a one-parameter family of straight lines with the parameter ξ. The envelope of this family of lines is a caustic curve.[1] To obtain the envelope, we differentiate eq. (1) with respect to ξ, $' = d/d\xi$,

$$a'(\xi)x + b'(\xi)y = c'(\xi). \tag{2}$$

The solution $x = x(\xi)$, $y = y(\xi)$ of eqs. (1) and (2) is the caustic curve in parametric form.[3]

Consider first the family of double-intercept rays, and refer to Fig. 11a. Here normal vectors to the curves are denoted by **n**, tangent vectors by **t**. The ray is first reflected from the lower curve at the point $[\xi, -g(\xi)]$.

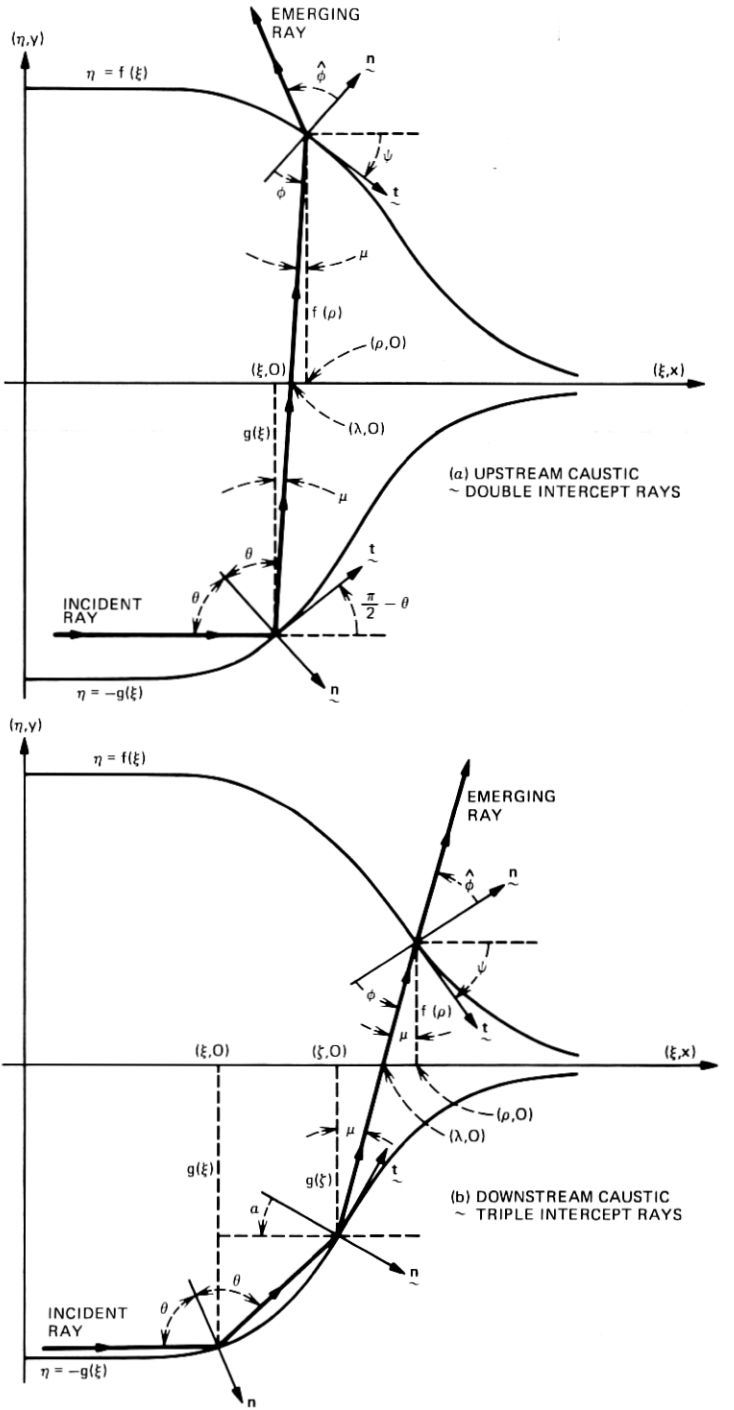

Fig. 11—Nomenclature used for the analysis of the caustic loci and for the ray-tracing calculations. All angles are positive measured in the counterclockwise sense.

Since the angle of incidence equals the angle of reflection, elementary geometry yields

$$\cot\theta = \tan\left[\frac{\pi}{2} - \theta\right] = -g'(\xi), \tag{3}$$

$$\theta' = g''(\xi)\sin^2\theta, \tag{4}$$

$$\mu = 2\theta - \frac{\pi}{2}. \tag{5}$$

Equation (4) is obtained by differentiating eq. (3), and eqs. (3) and (4) together determine $\theta(\xi)$ and $\theta'(\xi)$. Note that $g'(\xi) < 0$, so (3) determines $\theta(\xi)$ as an angle in the first quadrant. The use of eq. (5) for μ and simple trigonometry show that

$$\lambda = \xi - g(\xi)\cot 2\theta. \tag{6}$$

The ray next intersects the upper curve at the point$[\rho,f(\rho)]$. Observing the triangle with vertices $(\lambda,0)$, $(\rho,0)$, and $[\rho,f(\rho)]$, and making use of (5), we find

$$\rho - \lambda = -f(\rho)\cot 2\theta. \tag{7}$$

Since θ and λ are known functions of ξ from (3) and (6), we can determine $\rho(\xi)$ as the solution of (7). If eq. (7) is differentiated with respect to ξ and eqs. (3), (4), and (6) are used, it can be shown that

$$\rho'(\xi) = \left[-g'(\xi) - \frac{g''(\xi)}{g'(\xi)}\{g(\xi) + f(\rho)\}\right] \times \left[\sin 2\theta + \frac{df}{d\rho}(\rho)\cos 2\theta\right]^{-1}. \tag{8}$$

Next, by definition,

$$\tan\psi = \frac{df}{d\rho}(\rho), \tag{9}$$

and by differentiating (9) we get

$$\psi' = \frac{d^2f}{d\rho^2}(\rho)\rho'\cos^2\psi. \tag{10}$$

Simple geometry and Snell's law require that

$$\phi = \frac{\pi}{2} - \psi - 2\theta, \qquad \phi' = -\psi' - 2\theta', \tag{11}$$

$$\sin\hat{\phi} = n\sin\phi, \qquad \hat{\phi}' = (n\cos\phi/\cos\hat{\phi})\phi', \tag{12}$$

where n is the index of refraction of the glass. The equation of the emerging ray is

$$(x - \rho)\cos(\hat{\phi} + \psi) + (y - f(\rho))\sin(\phi + \psi) = 0. \tag{13}$$

If eq. (13) is differentiated with respect to ξ and eq. (9) is used, we get

$$-(x - \rho) \sin(\hat{\phi} + \psi) + [y - f(\rho)] \cos(\hat{\phi} + \psi) = F(\xi), \qquad (14)$$

where

$$F(\xi) = (\rho' \cos \hat{\phi})/\{(\hat{\phi}' + \psi') \cos \psi\}. \qquad (15)$$

Equations (13) and (14) can be solved for x and y to give the parametric equations of the caustic curve

$$x(\xi) = \rho - F(\xi) \sin(\hat{\phi} + \psi), \qquad y(\xi) = f(\rho) + F(\xi) \cos(\hat{\phi} + \psi). \qquad (16)$$

We evaluated $x(\xi)$ and $y(\xi)$ for the double-intercept rays by choosing a value of ξ and then successively determining θ, θ', ρ, ρ', ψ, ψ', ϕ, ϕ', $\hat{\phi}$, and $\hat{\phi}'$ from eqs. (3) through (12). These values were then used to determine $x(\xi)$ and $y(\xi)$ from (15) and (16). Values of $x(\xi)$ and $y(\xi)$ were evaluated at a number of closely spaced values of ξ and then plotted. The treatment of the triple-intercept rays, shown in Fig. 11b, uses the same type of argument. The calculations were carried out on a Honeywell 6000 digital computer. Most of the calculations involved only the use of standard trigonometric subroutines and either the Newton-Raphson method[4] or Brent's algorithm.[5]

The actual profile functions were approximated by sixth-order B-splines[6] possessing four continuous derivatives (a sixth order B-Spline is a piecewise polynomial of degree five). The approximations were obtained by making least squares fits of the B-Splines to the original profile data measured with the Nikon comparator. The fitting was done using an algorithm and subroutine developed by N. L. Schryer of Bell Laboratories.

In forming the caustic of double-intercept rays, only those rays were employed that intercepted the curve $\eta = -g(\xi)$ once and made an angle less than the critical angle with the normal to the surface at its intersection with the curve $\eta = f(\xi)$. Similarly, in forming the caustic of triple-intercept rays, only those rays were used that intercepted the curve $\eta = -g(\xi)$ twice in succession and made an angle less than the critical angle with the normal to the curve $\eta = f(\xi)$ on intersecting it.

In Figs. 12a and 12b, we show the caustics for sample 1 which lie in the 6–12 initial plane. This is the same sample shown in Fig. 1, although the initial plane of Fig. 1 is not the 6–12 plane. In both Figs. 12a and 12b, $f(\xi)$ is profile 6 and $g(\xi)$ is profile 12. Only those caustics corresponding to rays initially incident on profile 12 are shown. These caustics are representative of all those we have calculated, although of course there are important differences of detail. In both figures the heavy curves are the caustics, while the lighter straight lines are typical rays emerging from their point of tangency with the caustic.

For sample 1, all the incident rays were totally internally reflected at

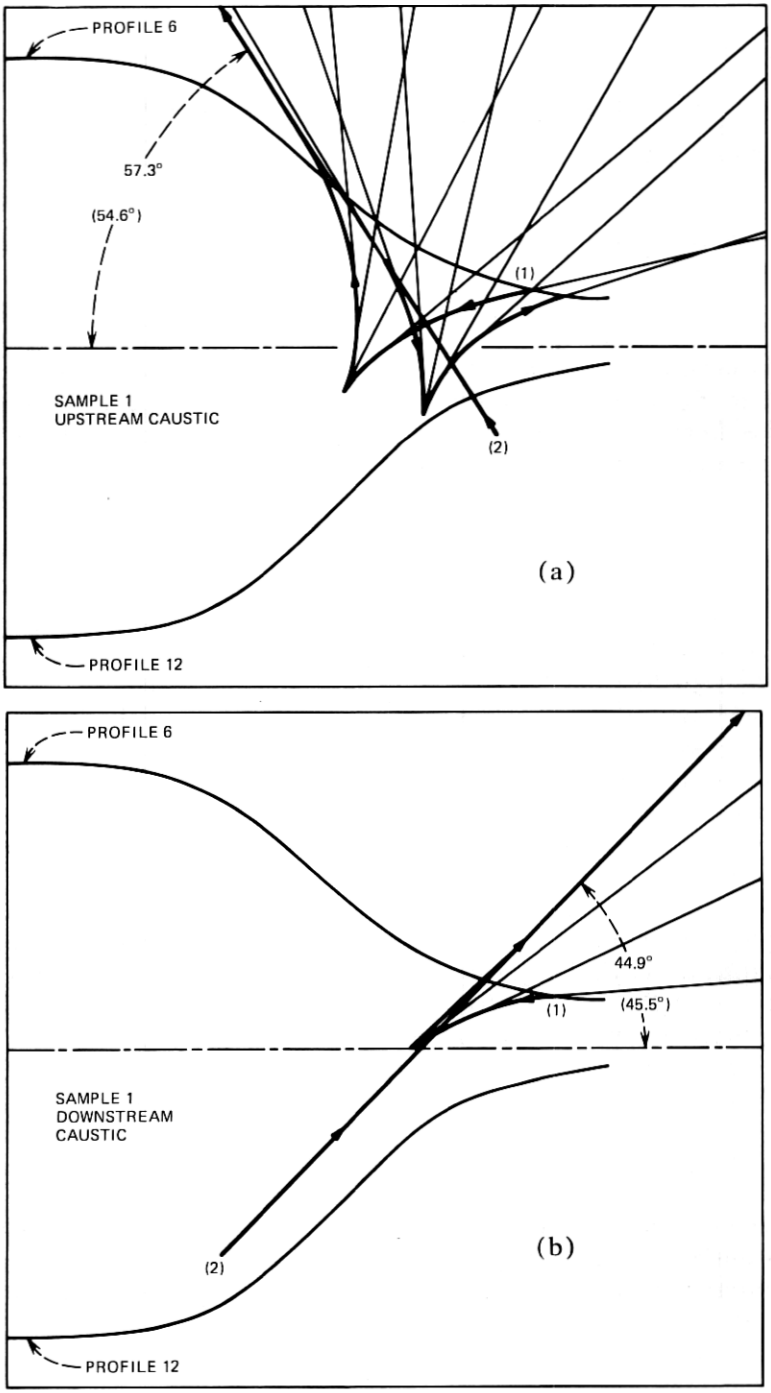

Fig. 12—Calculated loci of the upstream and downstream caustics in sample 1. The observed far-field caustic angles are given in parentheses.

their first intercept with the surface for the double-intercept rays, and for the first two consecutive intercepts for the triple-intercept rays. Sample 1 had a preform radius $r_0 = 3.242$ mm, and all the incident rays of the double-intercept family of Fig. 12a lay in the strip $0.160\, r_0 \leqq g(\xi) \leqq 0.929\, r_0$, while all the incident rays of the triple-intercept family of Fig. 12b lay in the strip $0.942\, r_0 \leqq g(\xi) \leqq 0.973\, r_0$.

The caustic curves themselves for both the double- and triple-intercept families consist of two branches. The point of the caustic $[x(\xi),y(\xi)]$ in Fig. 12a, which corresponds to the smallest permissible value of ξ, is labeled (1). As ξ increases, the caustic is traced out in the direction shown by the arrows. It has a cusp below the axis of the preform and then emerges from side 6 and goes to infinity in the direction shown. The second branch returns from infinity at the bottom of the figure [shown schematically by (2)], crosses the lower boundary, has two cusps, and ends near the upper boundary. Note that all the finite cusps are virtual, that is inside the silica. The important point to note is that the tangents to both branches of the curve at infinity are parallel and are superimposed. This part of the caustic, which goes to infinity, we referred to earlier as the emergent or far-field upstream caustic. The emergent rays thus form a fan parameterized by ξ. As ξ increases, the rays, initially pointing downstream, rotate counterclockwise until they reach the limiting position tangent to the caustic at infinity, and then rotate back in a clockwise direction. It is the accumulation of the rays in the direction of the tangent to the caustic at infinity which produces the observed far-field image. The angle obtained from our calculations between the axis of the preform and the tangent to the caustic at infinity was 57.3°. The measured value was 54.6°. The caustic curve of the triple-intercept family of rays (Fig. 12b), although simpler, has the same general structure. The calculated value of the angle between the axis of the preform and the tangent to the caustic at infinity was 44.9° and the measured value was 45.5°.

Although we have consistently talked about caustic curves, there is also a caustic surface, which is the envelope of the caustic curves. Although this caustic surface is not symmetric about the preform axis, it can nevertheless be roughly visualized by rotating the caustic curves in Figs. 12a and 12b about the preform axis. The upstream caustic surface describes reasonably well the upstream separation between the light and dark regions shown in Fig. 1. However, the downstream separation between the light and dark regions in the drawdown zone has not been completely explained on the basis of the caustics we have been studying.

In Table II we have summarized the calculated and observed angles between the preform axis and the tangents to the caustics at infinity for the four samples studied. The station number labels the profile curve

Table II — A comparison of the observed and calculated caustic angles for four drawdown samples

		Caustic Angles in Degrees, θ			
		Upstream		Downstream	
Sample	Station	Calculation	Observation	Calculation	Observation
1	3	54.5	46.1	46.2	49.4
	6	57.3	54.6	44.9	45.5
	9	75.3	72.5	37.3	40.0
	12	65.3	54.2	42.9	46.8
$2\theta_A = \theta_3 + \theta_9$		129.8	118.6	83.5	89.4
$2\theta_A = \theta_6 + \theta_{12}$		122.6	108.8	87.8	92.3
2	3	No emerging caustic,	(46.2)	NC*	57.2
	6	extinction boundary	(47.6)	49.2	53.0
	9	at 47	(46.9)	NC	56.8
	12		(48.8)	64.6	65.2
$2\theta_A = \theta_3 + \theta_9$		No caustic	(93.1)	NC	114.0
$2\theta_A = \theta_6 + \theta_{12}$		No caustic	(96.4)	113.8	118.2
3	3	48.0[64.1]	46.0[63.4]	83.6	78.3
	6	NC	43.7[63.4]	NC	81.5
	9	49.0[65.1]	45.5[61.3]	80.7	84.6
	12	NC	45.5[62.5]	NC	84.6
$2\theta_A = \theta_3 + \theta_9$		97.0[129.2]	91.5[124.7]	164.3	162.9
$2\theta_A = \theta_6 + \theta_{12}$		NC	89.2	NC	166.1
4	3	NC	101.0	NC	29.0
	6	86.5	86.0	41.9	39.5
	9	NC	86.6	NC	37.2
	12	104.7	105.0	25.5	26.1
$2\theta_A = \theta_3 + \theta_9$		NC	187.6	NC	66.2
$2\theta_A = \theta_6 + \theta_{12}$		191.5	191.0	66.6	65.5

* NC means not calculated.

through which the observed rays emerge. In Fig. 5b we show the observed and calculated caustics in the 6–12 plane for sample 4. The agreement between theory and experiment is very good in most cases. Several cases are of special interest. No upstream caustic was observed in sample 2, and none was exhibited by the model. Two upstream caustics were observed in sample 3, and the model also exhibited these two caustics and the agreement between the model and experiment is good. In short, we feel that our geometrical optics model has explained a variety of complicated effects very well.

V. DISCUSSION

Table II shows the agreement between the experimental observations of the emitted caustic angles and the predicted values. Most of the comparisons agree within 6 percent. The only exceptions are the upstream caustics at the 3 and 12 o'clock orientations on sample 1. As explained in Section 3.3, these upstream caustics are associated with an approach to the critical angle where the geometrical dependence becomes

exaggerated beyond the precision of the profile data. In other words, the accuracy of the profile measurement is insufficient to compute properly the emerging angles, $\hat{\phi}$, when the differential quantity, $d\hat{\phi}/d\phi$, is so large and changing so rapidly, see Fig. 8. The above exceptions are related to a singularity in the dependence of the upstream caustic on the maximum profile slope at which the caustic disappears. The caustic vanishes when the maximum slope approaches unity, causing it to intercept the opposite side of the drawdown at an angle greater than the critical and thus be reflected internally. At a slightly greater slope, depending on the index of refraction, the incidence of the internal rays at the first side is less than the critical angle. Consequently, most of the incident light will refract from the glass instead of reflecting across the drawdown. The low-intensity light which is reflected internally also forms a caustic originating at the inflexion point. That caustic crosses the drawdown zone at even steeper angles as the maximum slope increases until it intercepts the opposite side at an angle less than the critical angle and emerges. For sufficiently steep gradients the fan of light behind the caustic can also arrive at angles incident to the surface within the critical angle and emerge to form yet another caustic by refraction from the curved profile of the drawdown, e.g., sample 3.

The angles given for the upstream caustic directions of sample 2 are shown parenthetically in Table II because they represent limiting rays governed by internal reflection rather than caustics. As such they can be expected to equal angles very nearly tangent to the maximum slopes, Table I, and/or angles complimentary to the critical angle, 43.2°. The observed values satisfy these criteria quite well. The bracketed values given in Table II represent calculated and observed caustic angles for the second upstream caustic generated by sample 3 and discussed earlier.

A comparison of the measured included caustic angles with the average tapers computed for each orthogonal profile pair is shown in Fig. 13. There it can be seen that as the taper, L/D and β decrease, e.g. with slower drawing rates or higher temperatures, the included angles of the upstream caustics likewise decrease and those of the downstream caustics increase. In addition we have found that, aside from the anomalous extinction when β is near the critical angle, the number of caustics increases as L/D decreases, and the interaction between reflected and refracted light wave fronts becomes more complex. Conversely, as L/D increases, the included angle of the downstream caustic decreases continuously until that caustic disappears entirely by internal reflection. In extreme cases, such as long tapered drawdowns from furnaces, the upstream caustic rotates so far downstream that it also reflects internally, and ultimately no light is emitted. In that case ($L/D \gg 1$), the drawdown acts as a waveguide for the light entering the preform and

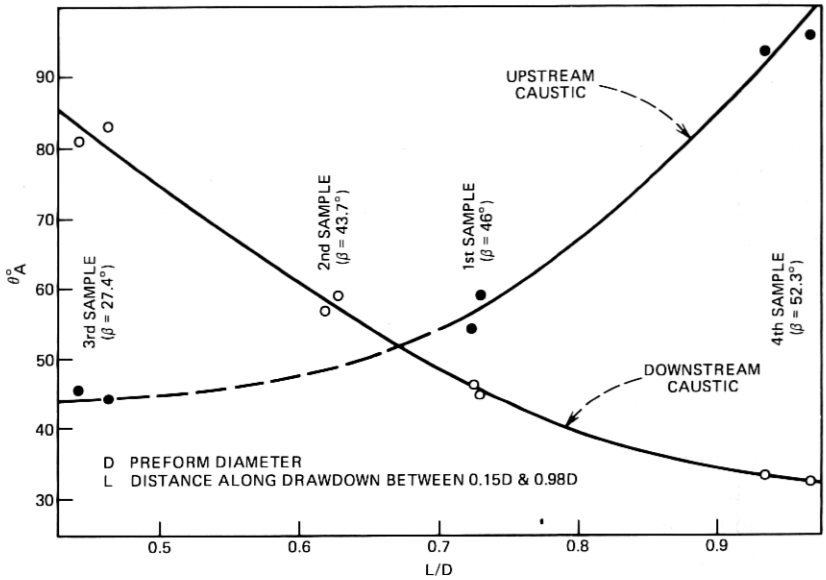

Fig. 13—Correlation of the included angles of the far-field caustics with the drawdown taper.

transmits all of it into the drawn fiber. This behavior is actually observed in furnace-drawn fiber drawdowns.

VI. SUMMARY

Our studies have shown that two unique families of caustics can be formed by light emanating from within a drawdown. We have chosen to designate these two families as "upstream" and "downstream" caustics; their character is rigorously defined in terms of the number of intercepts the trajectory makes with the drawdown profile. A very gradually tapered drawdown will emit no light and no caustics are formed. As the slope increases, light will appear in a downstream direction where the two intercept rays strike the opposite side at less than a critical angle, eventually forming an "upstream" caustic headed *downstream.* As the slope increases still further, the propagation direction of the caustic rotates upstream. Soon the downstream caustic appears and progresses in a similar manner with increasing slope. A singularity in the dependence of the upstream caustic on the maximum profile slope occurs near unity, causing the caustic to disappear by internal reflection.

External illumination of the drawdown zone by a collimated beam produces a far-field caustic pattern. This reflection caustic provides a direct measure of the maximum slope of the drawdown. Obviously the difference between the behavior of the externally illuminated caustic

and the internally illuminated downstream caustic, which is also slope related, will evolve from the optical properties of the glass and the secondary geometrical properties of the drawdown profile.

We have also found that the far-field images of all the caustics exhibit asymmetries related to geometrical asymmetries of the drawdown zone. The downstream caustic asymmetry is a fairly direct measure of the asymmetry of the slopes of the opposite drawdown profiles, while the upstream caustic responds to a more complicated interplay of geometrical factors. The enhanced geometrical sensitivity at incident angles near the critical produces an exaggerated asymmetry sensitivity in far-field upstream caustic images.

VII. ACKNOWLEDGMENTS

We wish to thank the following individuals for their assistance and helpful suggestions: S. I. Feldman, R. E. Jaeger, N. L. Schryer, E. A. Sigety, and J. R. Simpson.

APPENDIX

Estimations of accuracy

Profile measurements of the solidified samples were made on a Nikon optical comparator. Data were recorded every 0.13 mm (0.005 in.) along the profile to an accuracy of 0.005 mm (0.0002 in.). These data were used in the geometrical ray tracing procedures and the numerical computations. During the experiments in which the caustic images were recorded and/or measured, translatory motions were determined to an accuracy of 0.025 mm. All detailed analysis of the caustics were made by direct measurement of the images displayed on suitable screens. The caustic location was established with a metric scale and a vernier rule. We estimate that, with the screen in a horizontal position (e.g., position 1 or 3, Fig. 2), the caustics can be located, with respect to the preform, to within ± 0.1 mm vertically and ± 0.2 mm horizontally. When the beam size was reduced by slits or iris diaphragms, the aperture was measured to within a 0.001 mm with a traveling microscope.

Measurements of the maximum gradient of the drawdown profile using the external reflected caustic (see Section II), were found to be repeatable to within 1 percent. These results were more easily and more accurately obtained by the caustic technique than by analysis of the data obtained by the Nikon comparator.

REFERENCES

1. M. Born and E. Wolfe, *Principles of Optics*, Chap. III, London: Pergamon Press, 1959.

2. *Handbook of Chemistry and Physics,* 55th Edition, CRC Press, 1974.
3. D. J. Struik, *Lectures on Classical Differential Geomtry,* Cambridge, Mass.: Addison-Wesley, 1950, page 73.
4. R. W. Hamming, *Numerical Methods for Scientists and Engineers,* New York: McGraw-Hill, 1962, page 81.
5. R. P. Brent, *Algorithms for Minimization Without Derivatives,* New Jersey: Englewood Cliffs, Prentice-Hall, 1973, page 48.
6. H. B. Curry and I. J. Schoenberg, "On Polya Frequency Functions IV," J. Anal. Math., *17,* 1969, pp. 77–107.